Three-Dimensional Chemical Analysis with Synchrotron Tomography at Multiple X-ray Energies: Brominated Aromatic Flame Retardant and Antimony Oxide in Polystyrene

Kyungmin Ham,[†] Hua Jin,[‡,▼] Riyadh Al-Raoush,[§] Xiaogang Xie,[||] Clinton S. Willson,[§] Gary R. Byerly,[||] Larry S. Simeral,[⊥] Mark L. Rivers,[#] Richard L. Kurtz,[‡] and Leslie G. Butler*[,▲]

Center for Advanced Microstructures and Devices, Louisiana State University, 6980 Jefferson Hwy, Baton Rouge, Louisiana 70806, Department of Physics and Astronomy, Louisiana State University, Baton Rouge, Louisiana 70803, Department of Civil and Environmental Engineering, Louisiana State University, Baton Rouge, Louisiana 70803, Department of Geology and Geophysics, Louisiana State University, Baton Rouge, Louisiana 70803, Albemarle Corporation, Process Development Center, Gulf States Road, P.O. Box 341, Baton Rouge, Louisiana 70821, Consortium for Advanced Radiation Sources and Department of Geophysical Sciences, University of Chicago, Chicago, Illinois 60439, and Department of Chemistry, Louisiana State University, Baton Rouge, Louisiana 70803

Received October 18, 2003. Revised Manuscript Received July 16, 2004

Synchrotron X-ray tomography is used to image, at 3.34 μm resolution, a mixture containing high-impact polystyrene (HIPS) and a two-component flame retardant, a brominated phthalimide dimer (Saytex BT-93), and a synergist, antimony oxide (Sb_2O_3). Complete tomography data sets were acquired at seven X-ray energies in the range of 12−40 keV, closely spanning Br and Sb 1s electron binding energies at 13.474 and 30.491 keV, respectively. Data acquisition required 8 h. Quantification is done for a representative subvolume of 0.582 mm^3 containing 250^3 cubic volume elements (voxels) which is fitted to a model for X-ray voxel linear attenuation coefficient, yielding the three-dimensional concentration distribution of the flame retardant and the synergist. With successive thresholding, a particle size distribution algorithm yields regions of low flame retardant concentration—a potential safety concern—and regions of excessively high flame retardant concentration—a waste of an expensive product.

Introduction

Materials characterization with imaging requires a balance of many factors: sample preparation, resolution, dimensionality, image processing, and feature analysis. Sample preparation can range from microtome cutting[1−3] and evaporation of a gold overlayer to crude cuts with a penknife. Resolution can range from subnanometer in probe microscopy experiments to millimeters in acoustic and NMR imaging. Image dimensionality is most commonly two, although 1D imaging has an important niche for time-dependent properties such as real-time observation of surface reactions.[4] Often overlooked is k-space imaging[5] which can efficiently yield parameters such as average feature spacing. Three-dimensional imaging is attractive, but the data set sizes are formidable, on the order of gigabytes. As each volume element (voxel) is imaged, a single parameter is obtained, usually the X-ray linear attenuation coefficient. In the distant future, one might obtain the Cartesian coordinates, momentum, and phase space information of each particle in a material. However, with today's instrumentation, one measures the average X-ray absorption, acoustic loss, or NMR signal strength voxel by voxel. Hence, the parameter measured must be matched to the particular materials science question to be addressed.

Recently, synchrotron microtomography has developed into a fast, reliable method for three-dimensional

* To whom correspondence should be addressed. E-mail: lbutler@lsu.edu.
[†] Center for Advanced Microstructures and Devices, Louisiana State University.
[‡] Department of Physics and Astronomy, Louisiana State University.
[§] Department of Civil and Environmental Engineering, Louisiana State University.
[||] Department of Geology and Geophysics, Louisiana State University.
[⊥] Albemarle Corporation.
[#] University of Chicago.
[▲] Department of Chemistry, Louisiana State University.
[▼] Current address: Department of Materials Science & Engineering, Northwestern University, Evanston IL 60208.

(1) Marschallinger, R. *Scanning* **1998**, *20*, 65−73.
(2) Jastrow, H.; Vollrath, L. *Clin. Anat.* **2003**, *16*, 44−54.
(3) Center, P. S. The Visible Human Project at the Pittsburgh Supercomputing Center. http://www.psc.edu/biomed/research/VH/PVB/ (accessed September 2003).
(4) Butler, L. G.; Cory, D. G.; Dooley, K. M.; Miller, J. B.; Garroway, A. N. *J. Am. Chem. Soc.* **1992**, *114*, 125−135.
(5) Barrall, G. A.; Frydman, L.; Chingas, G. C. *Science* **1992**, *255*, 714−717.

10.1021/cm0350333 CCC: $27.50
Published on Web 09/15/2004

imaging of materials at the micrometer distance scale.[6−12] In a few hours, image data sets consisting of 250^3 to 1024^3 voxels can be acquired and transformed into absorption data. After data acquisition, a challenging problem is 3D image analysis. For large, well-defined objects, a combination of slice-by-slice display and manual tracing is effective.[13] For two phase systems having large contrast, 3D absorption data are converted into 3D binary images (black−white or 0−1 images).[14] Physical structures in 3D binary images such as channels and pores are characterized with routines such as a medial axis search tool, 3DMA.[15−18] Recently, the physics of grain growth for an aluminum−tin alloy was used to identify voxels as either $Al_{98}Sn_2$ grains or the Sn film between grains.[19] Also, lung structures and structures within the brain have been extracted from 3D images.[20,21] Very recently, the pore structure in polyvinyl chloride foams has been studied with tomography and a mean intercept technique.[22]

However, many objects are not easily converted into binary images, for example, any material having a distribution of concentrations such as additives blended with a polymer matrix or any other sample without clearly resolved peaks in a histogram of linear attenuation coefficients. Herein, we evaluate multi-X-ray energy synchrotron tomography for 3D concentration analyses. Seven images were acquired from 12 to 40 keV and the polymer blend components were analyzed based on the X-ray absorptions of pure phases. Sample preparation is minimal, the experiment requires 8-h of instrument time, and data processing is straightforward. The heterogeneous distributions of a flame retardant, a brominated aromatic, and its synergist, antimony oxide, are clearly and independently visualized. Based on these results, multi-X-ray energy imaging is widely applicable to compositional analysis. To the best of our knowledge, this work is the first complete application of multispectral X-ray imaging for 3D concentration analysis.

Structural features in X-ray absorption imaging are a consequence of characteristic elemental absorptions, and for the range of 2−100 keV, the energies and linear attenuation coefficients can be predicted based on elemental composition and sample density.[23] For example, grain structure in an aluminum−tin alloy is clearly visible based on the 16-fold greater X-ray mass absorption for Sn versus Al at 15 keV.[19] In our work, we seek the distribution of a brominated aromatic and finely powdered antimony oxide within a polystyrene sample. Since Br and Sb have K-edge absorptions at 13.474 and 30.491 keV, respectively, the sample was imaged at 12, 13.4, 13.5, 25, 30.43, 30.53, and 40 keV to yield seven data sets, with each reconstructed volume data set being 0.415 GB (1 GB = 2^{30} bytes). The objective of this work is data reduction to convert 2.905 GB of imaging data into 3D concentration maps.

Many consumer products—for example, the plastic housing of a computer CRT monitor—are made with high impact polystyrene (HIPS). By itself, this material will support combustion. As televisions were introduced into Great Britain, the incidence of household fires rose dramatically, until flame retardants were introduced.[24] Today, a common flame retardant is a mixture of a brominated aromatic and antimony oxide, both present at high loading levels.[25−27] The plastic CRT monitor shell can be as much as 30% bromine by mass. There are three issues with brominated aromatic flame retardants. First, the solubility of the brominated aromatic with high impact polystyrene (HIPS) varies with the molecular structure of the brominated aromatic. Good miscibility is required, else the stability of the final product can be poor. Second, brominated aromatics are difficult to observe with the more common spectroscopic methods typically used for polymer blend characterization. Solid-state ^{13}C NMR is often used for polymer studies, yet the quadrupolar bromine nucleus causes such line broadening of the ^{13}C resonances that miscibility is difficult to ascertain,[28] hence, the use of the relatively uncommon technique of ^{81}Br NQR.[29,30] While, in principle, NMR imaging could be used to study miscibility and possible leaching of flame retardants from the polymer blend, synchrotron microtomography is judged to be a faster and more accessible technique. Commercial brominated flame retardants (Figure 1) have somewhat different abilities to dissolve in a matrix like high-impact polystyrene (HIPS). An aromatic ether, 1-(2,3,4,5,6-pentabromophenoxy)-2,3,4,5,6-pentabromobenzene (Saytex 102), is miscible in HIPS, based on X-ray scattering and ^{81}Br NQR. However, a somewhat

(6) Spanne, P.; Rivers, M. L. *Nucl. Instrum. Methods Phys. Res., Sect. B* **1987**, *B24−25*, 1063−1067.
(7) Flannery, B. P.; Deckman, H. W.; Roberge, W. G.; D'Amico, K. L. *Science* **1987**, *237*, 1439−1444.
(8) D'Amico, K. L.; Deckman, H. W.; Dunsmuir, J. H.; Flannery, B. P.; Roberge, W. G. *Rev. Sci. Instrum.* **1989**, *60*, 1524−1526.
(9) Deckman, H. W.; D'Amico, K. L.; Dunsmuir, J. H.; Flannery, B. P.; Gruner, S. M. *Adv. X-Ray Anal.* **1989**, *32*, 641−650.
(10) Dunsmuir, J. H.; Ferguson, S. R.; D'Amico, K. L. *Inst. Phys. Conf. Ser.* **1992**, *121*, 257−264.
(11) Spanne, P.; Thovert, J. F.; Jacquin, C. J.; Lindquist, W. B.; Jones, K. W.; Adler, P. M. *Phys. Rev. Lett.* **1994**, *73*, 2001−2004.
(12) Butler, L. G.; Owens, J. W.; Cartledge, F. K.; Kurtz, R. L.; Byerly, G. R.; Wales, A. J.; Bryant, P. L.; Emery, E. F.; Dowd, B.; Xie, X. G. *Environ. Sci. Technol.* **2000**, *34*, 3269−3275.
(13) Ellisman, M. H. National Center for Microscopy and Imaging Research: Xvoxtrace Version 2.3. http://ncmir.ucsd.edu/doc/Xvoxtrace-.html (accessed June 2003).
(14) Lohmann, G. *Volumetric Image Analysis*; Wiley-Teubner: New York, 1998.
(15) Lindquist, W. B.; Lee, S.-M.; Coker, D. A.; Jones, K. W.; Spanne, P. *J. Geophys. Res. B* **1996**, *101*, 8297−8310.
(16) Oh, W.; Lindquist, W. B. *IEEE Pattern Anal. Machine Intelligence* **1999**, *21*, 590−602.
(17) Al-Raoush, R. I.; Thompson, K.; Willson, C. S. *Soil Sci. Am. J.* **2003**, *67*, 1687−1700.
(18) Al-Raoush, R. I.; Willson, C. S. *J. Hydrol.* **2004**, in press.
(19) Krill, C. E., III.; Döbrich, K. M.; Michels, D.; Michels, A.; Rau, C.; Weitkamp, T.; Snigirev, A. A.; Birringer, R. *Proc. SPIE-Int. Soc. Opt. Eng.* **2002**, *4503*, 205−212.
(20) Wan, S. Y.; Ritman, E. L.; Higgins, W. E. **2002**, *32*, 55−71.
(21) Ratnanather, J. T.; Botteron, K. N.; Nishino, T.; Massie, A. B.; Lal, R. M.; Patel, S. G.; Peddi, S.; Todd, R. D.; Miller, M. I. Validating cortical surface analysis of medial prefrontal cortex. In *Neuroimage*, 2001; Vol. 14, pp 1058−1069.
(22) Elmoutaouakkil, A.; Fuchs, G.; Bergounhon, P.; Péres, R.; Peyrin, F. *J. Phys. D: Appl. Phys.* **2003**, *36*, A37−43.
(23) NIST, NIST XCOM: Photon Cross Sections Database. http://physics.nist.gov/PhysRefData/Xcom/Text/XCOM.html (accessed June 2003).
(24) Litzenburger, A. *Polym. Polym, Compos.* **2000**, *8*, 581−592.
(25) De Schryver, D.; Landry, S. D.; Reed, J. S. *Polym. Degrad. Stab.* **1999**, *64*, 471−477.
(26) Simonson, M. *Polym. Mater. Sci. Eng.* **2000**, *83*, 90−91.
(27) Albemarle, Albemarle Corp. Saytex brochure page. http://www.albemarle.com/saytexbro.htm (accessed June, 2003).
(28) Radloff, D.; Spiess, H. W.; Books, J. T.; Dowling, K. C. *J. Appl. Polym. Sci.* **1996**, *60*, 715−720.
(29) Mrse, A. A.; Lee, Y.; Bryant, P. L.; Fronczek, F. R.; Butler, L. G.; Simeral, L. S. *Chem. Mater.* **1998**, *10*, 1291−1300.
(30) Harwell, C. R.; Mrse, A. A.; Shelby, A. I.; Butler, L. G.; Hall, R. W. *J. Phys. Chem. A* **1999**, *103*, 8088−8092.

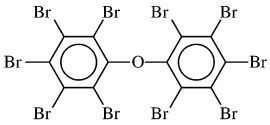

1-(2,3,4,5,6-pentabromophenoxy)-2,3,4,5,6-pentabromobenzene (Saytex 102)

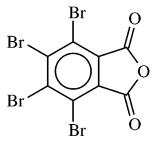

3,4,5,6-tetrabromophthalic anhydride (Saytex RB-49)

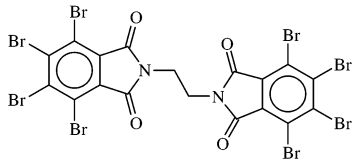

3,3',4,4',5,5',6,6'-octabromo-*N,N'*-ethylenediphthalimide (Saytex BT-93)

Figure 1. Representative flame retardants.

larger molecule, 3,3′,4,4′,5,5′,6,6′-octabromo-*N*,*N*′-ethylenediphthalimide (Saytex BT-93), appears to exist as microcrystalline domains dispersed in the HIPS matrix.[25,28,29]

The distribution of flame retardants in a polymer matrix is a particularly nice problem for multi-X-ray energy synchrotron tomography. Sample preparation is done with simple cutting, and not a microtome; a microtome's water or oil lubrication may wash flame retardants from the sample. The resolution needed to assess blend distribution is defined by the initial particle size; both the brominated aromatic and the antimony oxide are initially microcrystalline, thus requiring micrometer resolution. Image dimensionality could be k-space but 3D imaging is desired in this exploratory study. Last, each voxel must be analyzed for its composition: fraction polymer, fraction brominated aromatic, and fraction antimony oxide. This last requirement is the exceptional advantage of multi-X-ray energy imaging. The characteristic X-ray absorption spectra of each component can be fitted to the observed linear attenuation coefficients. Nominally, two X-ray energies would suffice to determine the two compositional unknowns; however, we have elected to over-determine the system.

In this manuscript, we will show how the 3D, element specific absorption data obtained using synchrotron X-ray tomography can be used to quantitatively determine the spatial characteristics and concentration values of a chemical mixture. Specifically, we will do the following: (1) calculate quantitative, absorption data from a series of 3D, high-resolution tomographic images obtained at multiple energies; (2) employ X-ray linear attenuation values for the chemical components as a function of energy; (3) use a least-squares fit technique on the data and parameters obtained from steps one and two to calculate chemical concentrations in each voxel in 3D space; and (4) utilize common image analysis and visualization techniques to quantify the concentration distribution and the correlation between flame chemicals in an effort to better understand the effectiveness of the blending techniques.

SEM, a more common 2D technique, is used to provide quantitative information on the heterogeneous distribution of the chemicals.

Experimental Section

Sample Preparation. Saytex BT-93 (3,3′,4,4′,5,5′,6,6′-octabromo-*N*,*N*′-ethylenediphthalimide) has a mp of 450−455° C. BT-93 and antimony oxide, Sb_2O_3, were mixed and shaken together and then melt-processed with high impact polystyrene at 220 °C. Sample compositions given in wt % can be converted to vol % via the pure component densities: ρ(BT-93) = 2.77 g/cm^3, $\rho(Sb_2O_3)$ = 5.67 g/cm^3, and ρ(HIPS) = 1.040 g/cm^3. The sample studied is 6.90 wt % Br (10.3 wt % BT-93) and 2.95 wt % Sb (3.53 wt % Sb_2O_3); corresponding to 4.25 vol % BT-93 and 0.714 vol % Sb_2O_3.

Scanning Electron Microscopy. For the electron microscope experiments, a thin section of the polystyrene blended with BT-93 and Sb_2O_3 was coated with a 20 nm thick carbon layer for energy-dispersive X-ray spectroscopy (EDS). EDS spectra and digital images based on X-ray mapping were acquired using a JEOL 840A scanning electron microscope (SEM) equipped with an ultrathin window EDS and a Macintosh G3/4Pi Spectral Engine II data acquisition and control system. NIST Desk Top Spectrum Analyzer (DTSA) and NIH Image software packages were used to display and process images. For the elemental distribution mapping, instrument parameters were 20 kV, 60 nA, and 20 μs dwell time per pixel, yielding images in 12-h of 1350 × 1070 pixels with a resolution of 1.1 μm. EDS spectra and secondary electron images (SEI) were acquired with 20 kV and 3 nA; the images are 1024 × 812 pixels with resolutions ranging from 10 to 20 nm.

Tomography. The GeoSoilEnviroCARS (GSECARS) bending magnet beam-line 13-BM-D (sector 13 at the Advanced Photon Source (APS) at Argonne National Laboratory) provides a fan beam of high brilliance radiation. When used with a monochromator (Si 111), energies in the range from 8 to 65 keV can be obtained with a beam width of 50 mm and height of 5 mm.[31] Transmitted X-rays are converted to visible light with a synthetic garnet (Ce:YAG) scintillator and the scintillator is imaged with a 5X Mitutoyo microscope objective focused onto a 12-bit CCD camera (Roper Scientific MicroMAX 5 MHz) 1300 × 1100 pixels, each 6.7 × 6.7 μm^2. The sample was cut into a rough cylinder with diameter of 1.3 mm and mounted with clay atop the tomography sample rotation stage. A total of 720 images were collected as the sample was rotated from 0° to 179.5° by 0.5° and then 0.25° to 179.75° by 0.5°. Over the course of the imaging experiment, the X-ray flux at the sample was stabilized to within a few percent with two mechanisms: The APS beam current was held constant by operation in "top-up mode". The orientation of the second crystal of the monochromator was fine- tuned based on feedback from an ion-chamber X-ray flux indicator mounted immediately upstream of the sample.

Each CCD image was converted to a transmission image with white field and average dark count correction. White field images were collected at intervals of 50 CCD images. The average dark field intensity was 85 counts. Sinograms were constructed, efforts were made to reduce zingers and ring artifacts, and the transmission values were converted to line integral of the absorption.[31] An attempt was made to measure the mass linear attenuation coefficients of pure BT-93 and Sb_2O_3 mounted in glass capillary tubes, but the total X-ray absorption was too great.

The slice reconstruction was done with a fast Fourier transform algorithm following a re-gridding from polar to Cartesian coordinate systems.[31] The slices were assembled into a single reconstructed volume of 650 × 650 × 515 volume elements, each element containing the value of the voxel linear attenuation coefficient. The voxel linear attenuation coefficient is equal to the mass attenuation coefficient (cm^2/g) × density (g/cm^3) × voxel dimension (cm).

The 2D FFT introduces small offset ($\leq 2 \times 10^{-5}$) and scale errors (less than or equal to ±10%) in the voxel linear attenuation coefficients, and these were corrected by rescaling

(31) Rivers, M. L.; Rivers, M. L. Tutorial Introduction to X-ray Computed Microtomography http://www-fp.mcs.anl.gov/xray-cmt/rivers/tutorial.html (accessed June 2003).

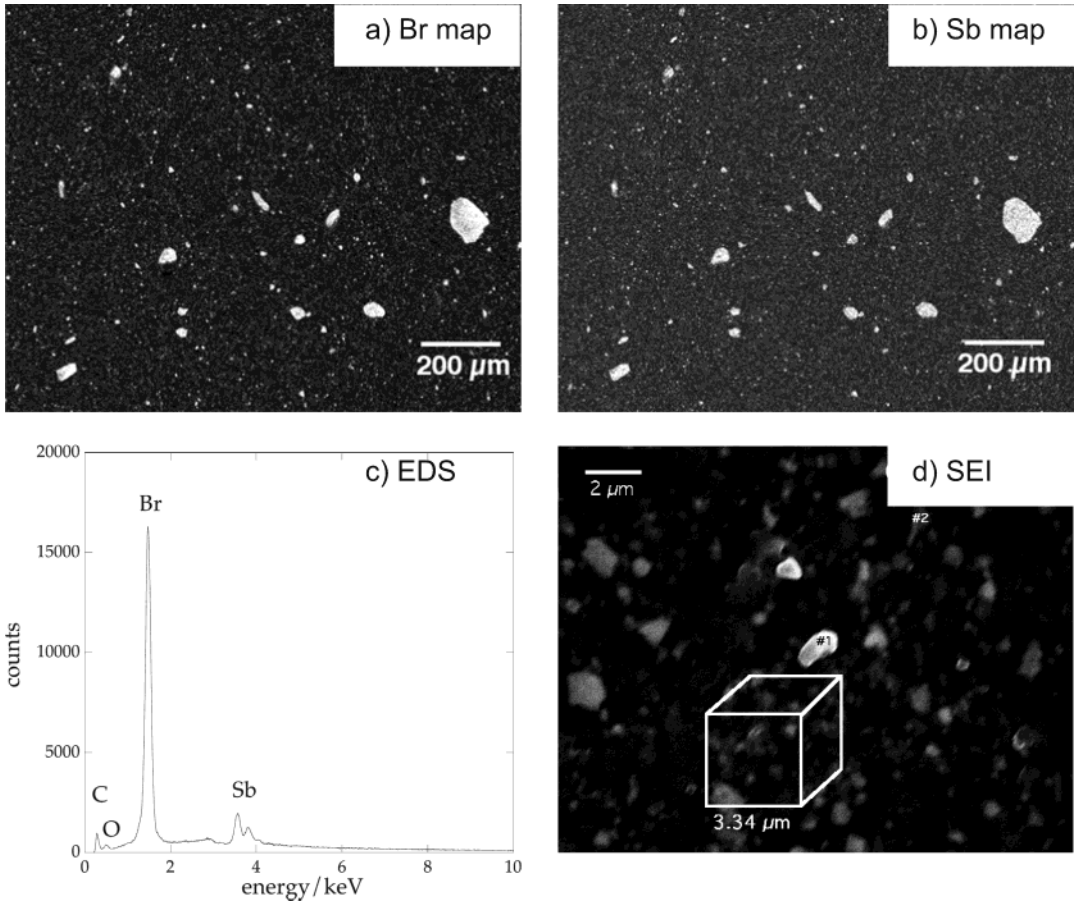

Figure 2. High-impact polystyrene blended with BT-93 and Sb_2O_3. (a) Br X-ray map. (b) Sb X-ray map. (c) EDS spectrum in a Br-rich area and (d) secondary electron image with a superimposed tomography volume element.

such that projections of representative slices yield voxel linear attenuation coefficients in agreement with the original absorption images. Note: when projections from the 3D data sets are calculated, only the voxels within the reconstructed Radon-defined circle were used; the absorption values for positions lying between the inscribed circle and the square defined by data storage were not used as these areas are not defined by the Radon transform. The scale factors were independently determined for each subvolume data set.

$$A_{xyzE} = \text{scale}_E \times A_{xyzE} + \text{offset}_E \quad (1)$$

Image Analysis. From each volume data set, a cubic subvolume of 250^3 voxels was selected for further analysis. Difference images showed no evidence of undesirable sample motion between images acquired at different X-ray energies. For each subvolume, a histogram of linear attenuation coefficients provided the first insight into the overall sample characteristics. In addition, the average linear attenuation coefficient was calculated as well as the maximum and the variance of linear attenuation coefficients. These calculations were done in a combination of IDL and Matlab programs. A constrained least-squares fit to the voxel linear attenuation coefficients (fit parameters constrained to have physically reasonable values) program was written in Matlab. Surface renderings of the 3D concentration maps were generated in IDL. Quicktime movie fly throughs were made either with Matlab or screen captures from IDL stitched together in Apple Authoring VR. The particle size distribution of BT-93- and Sb_2O_3-rich and depleted domains was obtained with a three-dimensional medial axis routine, 3DMA.[15]

Results and Discussion

Electron Microscopy. Electron microscopy yields qualitative and quantitative information about the heterogeneous distribution of BT-93 and Sb_2O_3 in the high impact polystyrene. The strong correlation between Br and Sb is obvious in the X-ray maps (Figures 2a and 2b) and in the energy-dispersive X-ray spectra (Figure 2c), a spectrum typical of the bright regions in Figure 2a. Four elements were detected, Sb, Br, O, and C, suggesting that this point is a blend of BT-93, Sb_2O_3, and possibly polystyrene. The element distribution shown in Figures 2a and 2b is consistent with the sample preparation; BT-93 and Sb_2O_3 are mixed and then extruded with high-impact polystyrene (HIPS). Quantitative measurement of flame retardant distribution is possible with data sets such as these, provided calibrations with pure phases are done and a statistically large area is measured. Such a study is quite laborious. For example, each measurement (Table 1) requires approximately 3−6 min of instrument time. A secondary electron image (Figure 2d) shows submicrometer grains embedded in the polystyrene matrix. A scale bar shows the SEI resolution and, for comparison, a cube representing the tomography resolution is superimposed upon the image.

Table 1. Compositions from Energy Dispersive X-ray Spectroscopy

position	BT-93/vol %	Sb_2O_3/vol %	HIPS/vol %
grain 1	41.6	4.5	53.9
grain 2	29.2	4.8	66.0
grain 3	27.5	0.4	72.1
matrix 1	2.5	0.6	96.9
matrix 2	2.6	0.8	96.6
matrix 3	3.5	0.9	95.6
matrix 4	2.2	0.6	97.2

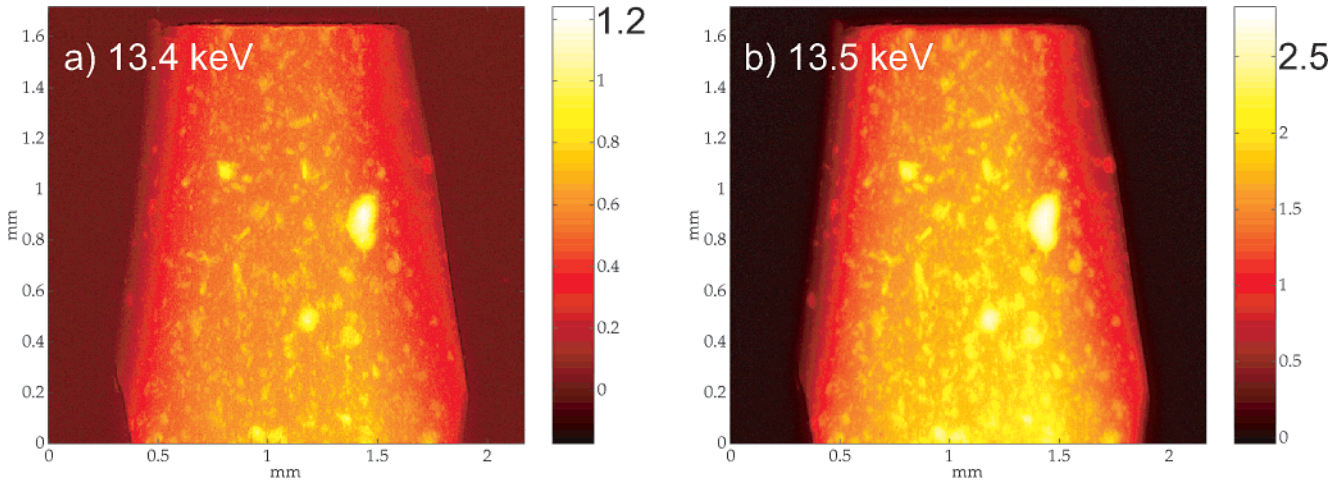

Figure 3. CCD images (white and dark field corrected) at (a) 13.4 keV and (b) 13.5 keV with color bars in absorption units. The rapid increase in X-ray absorption indicates dispersal of BT-93 within the polystyrene matrix as well as in domains on the order of 0.2 mm.

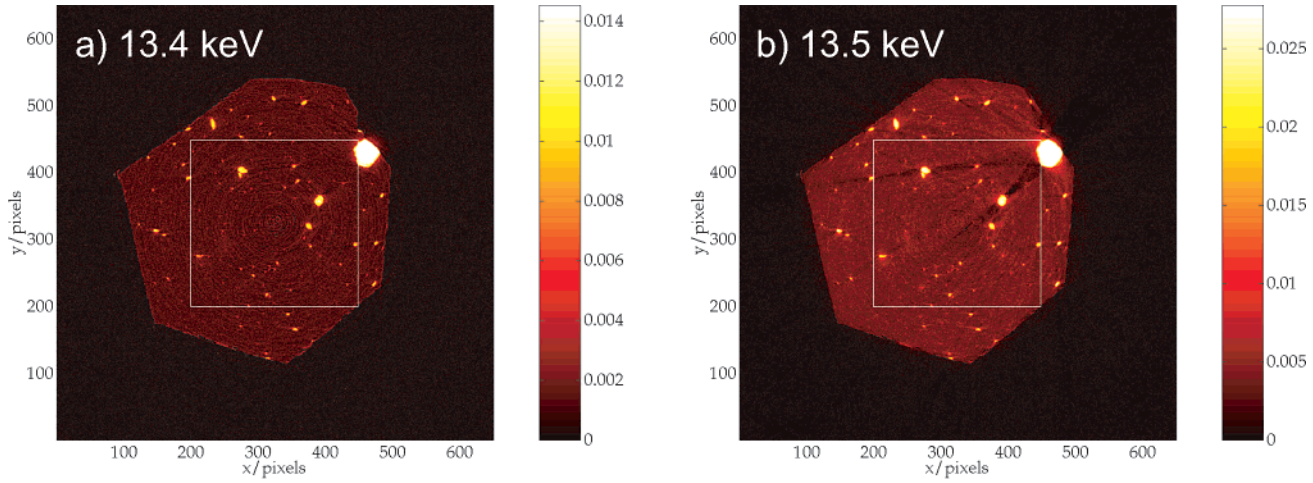

Figure 4. Reconstructed slices at (a) 13.4 keV and (b) 13.5 keV with color bars in units of voxel linear attenuation coefficients. The outline of the subvolume chosen for further analysis is shown (white box).

Images and Tomographic Reconstructions. The BT-93/Sb_2O_3/HIPS sample was imaged at seven different X-ray energies. Two pairs of X-ray energies closely span the Br and Sb X-ray absorptions, respectively, with the other three X-ray energies chosen at widely spaced intervals. Figure 3 shows the raw data, in absorption mode, and the dramatic change in X-ray absorption as a function of a small change in X-ray energy crossing the Br absorption edge. A similar change occurs at the Sb X-ray absorption edge at 30.491 keV with images acquired at 30.43 and 30.53 keV.

The tomographic reconstructions yield a rectilinear cube of data, 650 × 650 × 515 voxels, showing the sample and surrounding air. The color bars are in units of voxel linear attenuation coefficients, which can be related to the chemical composition for that voxel. A 250^3 voxel subvolume was extracted and used for further analyses; the subvolume outline is superimposed on the reconstructed images, as shown in Figure 4. This subvolume is quite large, consisting of over 15 million voxels with a volume of 0.582 mm^3. Seven subvolumes, one at each X-ray energy, were generated and used in the next phase of the analysis.

Histograms of Voxel Linear Attenuation Coefficients. A convenient method for visualizing the range and distribution of voxel linear attenuation coefficient of a large volume is a histogram. Shown in Figure 5 are the histograms for each of the seven subvolumes. There are several features of note. First, the dramatically increased voxel linear attenuation coefficient at 13.5 keV corresponds to the X-ray voxel linear attenuation coefficient by Br. Second, a similar, but less pronounced, increased voxel linear attenuation coefficient at 30.53 keV is due to Sb. Third, there is an overall decrease in voxel linear attenuation coefficient as the X-ray energy increases. Fourth, the shape of all histograms is roughly Gaussian and shows no appreciable bimodal character. The last is in stark contrast to simple two-phase materials which often show a bimodal distribution. The lack of bimodality has, heretofore, been an obstacle for the composition analysis of a material, hence, the seven different X-ray energies. The key features of each histogram are summarized in Table 2.

Mass attenuation coefficients are an additive, intrinsic property below 5 MeV.[23] The National Institute of Standards and Technology has compiled X-ray mass

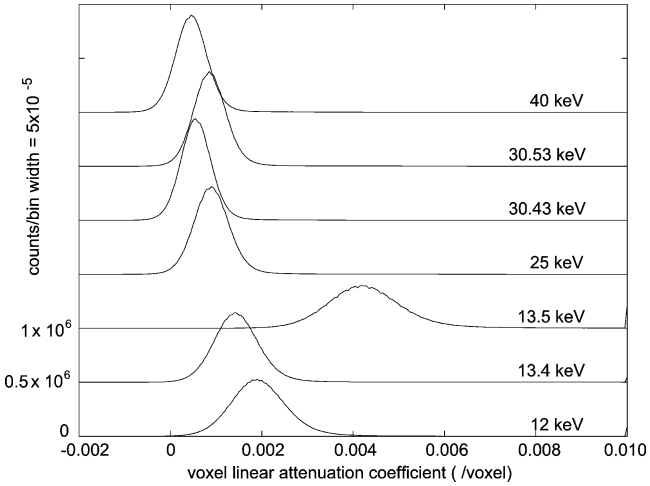

Figure 5. Histograms of voxel linear attenuation coefficients for the subvolume at seven X-ray energies. The subvolume contains $250^3 = 15\,625\,000$ voxels.

Table 2. Mean, Variance, and Maximum Voxel Linear Attenuation Coefficients at Various X-ray Energies

energy/keV	mean/10^{-3}	variance/10^{-3}	maximum/10^{-3}
12	2.07	1.2	25.13
13.4	1.55	0.93	21.07
13.5	4.49	1.8	36.44
25	0.949	0.56	10.41
30.43	0.590	0.43	7.11
30.53	0.913	0.54	11.21
40	0.479	0.42	6.44

Table 3. Calculated[a,b] Voxel Linear Attenuation Coefficients of Pure Components

energy (keV)	HIPS/10^{-3}	BT-93/10^{-3}	Sb_2O_3/10^{-3}
12	0.4688	19.15	142.4
13.4	0.3525	14.16	106.1
13.5	0.3462	91.41	104.0
25	0.1101	18.04	19.88
30.43	0.0907	10.55	11.74
30.53	0.0904	10.45	64.39
40	0.0757	4.98	32.19

[a] Voxel linear attenuation coefficients = mass attenuation coefficients (cm^2/g) × density (g/cm^3) × voxel dimension (cm). [b] We attempted to measure these values experimentally, but the high attenuation coefficients were not compatible with the capillary tube, about 1 mm i.d., used to hold the pressed, pure flame retardants.

attenuation coefficients for the elements and provides a computational tool for the prediction of attenuation coefficients for organics, minerals, and biological substances.[23] The conversion between X-ray mass attenuation coefficients and the voxel linear attenuation coefficient for a pure phase requires the density of the phase and the voxel size (length of a face). Table 3 lists the calculated voxel linear attenuation coefficients for polystyrene, BT-93, and Sb_2O_3 for the experimental energies used here. The images acquired at 13.5 and 30.53 keV are affected by XAFS effects, making the linear attenuation coefficients of Table 3 at those two X-ray energies imprecise by up to an estimated 10%.[32] The omission of XAFS effects on the final composition images is mitigated by the inclusion of additional images with high voxel linear attenuation coefficients at X-ray energies beyond the XAFS effects. A comparison of the

(32) Chantler, C.; Tran, C.; Barnea, Z.; Paterson, D.; Cookson, D.; Balaic, D. *Phys. Rev. A* **2001**, *64*, 062506.

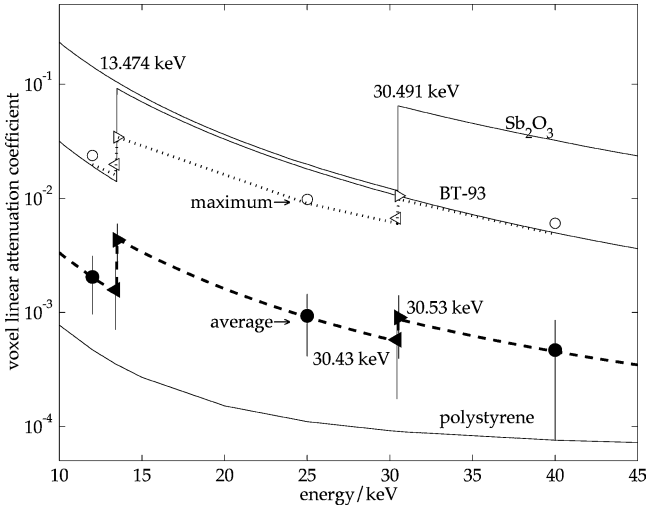

Figure 6. Experimental voxel linear attenuation coefficients: average (filled symbols), variance (vertical bars), and maximum linear attenuation coefficients (open symbols). The traces (solid lines) show the calculated voxel linear attenuation coefficient for three components: high impact polystyrene (HIPS), brominated aromatic (BT-93), and antimony oxide (Sb_2O_3). The dashed line shows the predicted voxel linear attenuation coefficient for the sample composition as measured by tomography. The dotted line shows the voxel linear attenuation coefficients for one voxel, the voxel having the largest X-ray absorption at 13.5 keV; this trace and similar are used to establish that no voxels contain only pure BT-93.

values in Table 3 and with maximum experimental voxel linear attenuation coefficients listed in Table 2 shows that polymer blending is effective; there are absolutely no voxels in the subvolume which consist exclusively of Sb_2O_3; at all X-ray energies, the maximum experimental voxel linear attenuation coefficient is less than that predicted for pure Sb_2O_3.

Graphically, we find it convenient to generate Figure 6, which compares the calculated pure phase voxel linear attenuation coefficient with the experimental average and maximum voxel linear attenuation coefficients. Casual inspection of Figure 6 shows blending; there are no voxels consisting of only pure Sb_2O_3. If there were such voxels, then the maximum experimental voxel linear attenuation coefficient would match the Sb_2O_3 calculated trace. Also of note in Figure 6 are the K-edge absorptions for Br and Sb, at 13.474 and 30.491 keV, respectively. The amplitude of the step functions is a function of the composition of the material. Some of the other preliminary interpretations of Figure 6 are as follows: The sample contains more BT-93 than Sb_2O_3. There are no other significant additives with atomic numbers between Br ($Z = 35$) and Sb ($Z = 51$). No voxels contain only pure BT-93; the voxel with the largest voxel linear attenuation coefficient at 13.5 keV has been identified and its values at the X-ray energies are shown in Figure 6 (dotted line) and is seen to be a mixture of BT-93, Sb_2O_3, and polystyrene. The other voxels associated with maximum voxel linear attenuation coefficient have been examined at the other X-ray energies and never show complete filling by BT-93. Since the subvolumes have reasonable values for voxel linear attenuation coefficients and are consistently aligned, the next step is to fit all voxel linear attenuation coefficients to three-dimensional BT-93 and Sb_2O_3 concentration distributions.

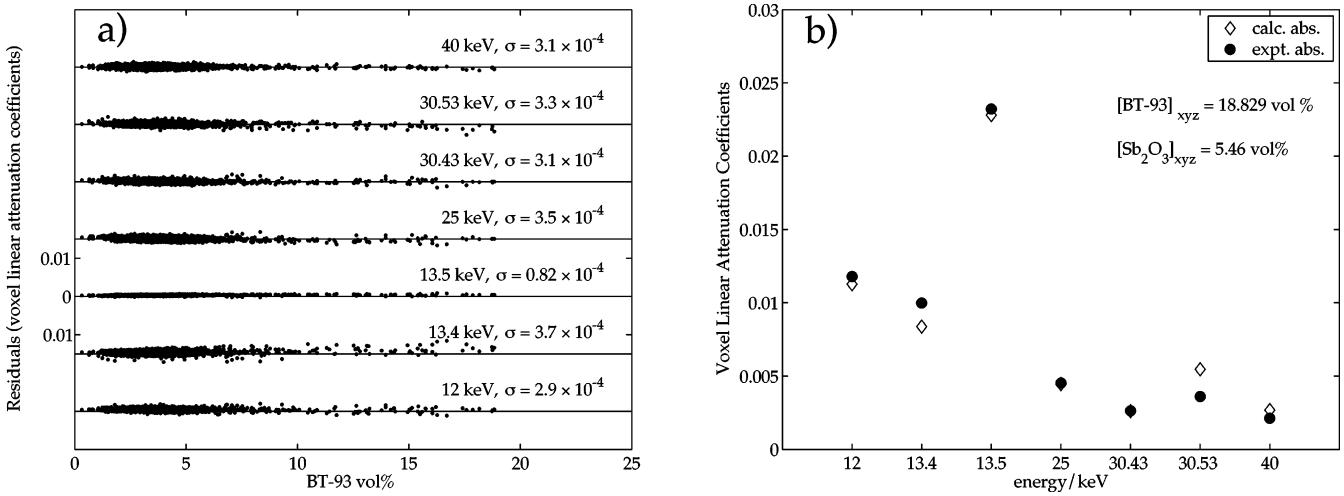

Figure 7. An assessment of the quality of the constrained least-squares fit: (a) 10^4 voxels chosen at random are fitted and the residuals displayed as a function of the fit parameter, BT-93 vol %. (b) An example of a fit at one voxel with high concentrations of BT-93 and Sb_2O_3 showing the good agreement between measured (filled symbol) and calculated (open symbol) voxel linear attenuation coefficients.

Least-Squares Fit of All Voxel Linear Attenuation Coefficients. X-ray mass attenuation coefficients are additive at energies below 5 MeV; thus, the following model is used,

$$A_{xyzE}^{\text{calc}} = [\text{BT93}]_{xyz} \times A_E^{\text{BT93}} + [\text{Sb}_2\text{O}_3]_{xyz} \times A_E^{\text{Sb}_2\text{O}_3} + (1 - [\text{BT93}]_{xyz} - [\text{Sb}_2\text{O}_3]_{xyz}) \times A_E^{\text{HIPS}} \quad (2)$$

where $[\text{BT93}]_{xyz}$, for example, is the thickness of BT-93 and we seek to minimize, voxel by voxel, the difference between the experimental and calculated voxel linear attenuation coefficients, A_{xyz} and A_{xyzE}^{calc}, respectively, by adjusting the concentration (vol %) of BT-93 and Sb_2O_3 in each voxel. For each voxel, the problem is overdetermined with seven equations and two unknowns, corresponding to the seven X-ray energies and the two unknown concentrations, respectively. However, noise in the data may yield physically impossible concentrations, either negative or in excess of 100%. For this reason, the fitting algorithm is a constrained nonlinear least-squares algorithm from the Matlab toolbox, a modification of the Levenburg-Marquardt algorithm; the constraint limits the range of the fit parameters, $[\text{BT93}]_{xyz}$ and $[\text{Sb}_2\text{O}_3]_{xyz}$ to lie between the physically possible values of 0−1, inclusive. The large number of fits, 250^3, required 2 weeks on a single processor campus mainframe and a few days when spread across several desktop computers.

Residuals are a standard method for assessing the quality of the fit, but with 7×250^3 residuals, the presentation is awkward. From within the subvolumes, sorted on the basis of a voxel linear attenuation coefficient at 13.5 keV, 10^4 voxels are selected and fitted with eq 2. The 7×10^4 residuals and the fit for one voxel are shown in Figure 7. There is no apparent systematic deviation in the residuals. The residual magnitude is on the order of 0.02 linear attenuation units, which is much smaller than the variance of the voxel linear attenuation coefficients listed in Table 2, a result consistent with a reliable fit.

Visualizations of Chemical Composition. The final results of the constrained least-squares fit are two 250^3 voxel cubes giving the three-dimensional distributions of BT-93 and Sb_2O_3. The average concentrations in these cubes are[25] [BT-93] = 3.831 vol % (9.343 wt %) and $[\text{Sb}_2\text{O}_3]$ = 0.638 vol % (3.185 wt %). The distribution can be presented in several formats: (1) rendering with color scale; (2) histogram of the voxel concentrations, and a (3) surface plot showing cross-correlation of BT-93 and Sb_2O_3 concentrations.

Each of these presentations will be given below.

A three-dimensional rendering, Figure 8, shows the heterogeneity in flame retardant distribution, in agreement with the 2D X-ray mapping images (Figure 2) and with the voxel linear attenuation coefficient variance for 13.5 and 30.54 keV tomography images (Table 2). Also, there is a strong correlation between the concentrations of BT-93 and Sb_2O_3, as was noted in the 2D X-ray mapping images (Figure 2). The unique feature of Figure 8 is the calibration of the image in terms of concentration. We note that the 2D X-ray mapping images yield the relative concentrations across a surface whereas Figure 8 shows the absolute concentrations throughout a volume. Admittedly, additional calibration work could improve the 2D X-ray mapping results, making those images quantitatively correct.

Histograms of Voxel Compositions. Three-dimensional renderings are attractive, but should be supplemented with alternative presentations. The human eye may not accurately compute an average composition. Therefore, a histogram presentation remains useful, as shown in Figure 9. For convenience, the *x*-axis plot ranges are proportional to the variance of the concentration distributions. Later in the analysis, we will focus on the voxels with very low concentrations, which are highlighted in red in Figure 9. Similarly, the voxels with very high concentrations are highlighted in blue.

Cross-correlations between components in a blend is an important issue. A high correlation may indicate a common mechanical path of the components or an affinity between components such as a chemical reaction leading to coprecipitation. The cross-correlation of BT-93 with Sb_2O_3 concentrations is examined with a contour plot, shown in Figure 10. Again, as was evident in the X-ray mapping images (Figure 2), there is an

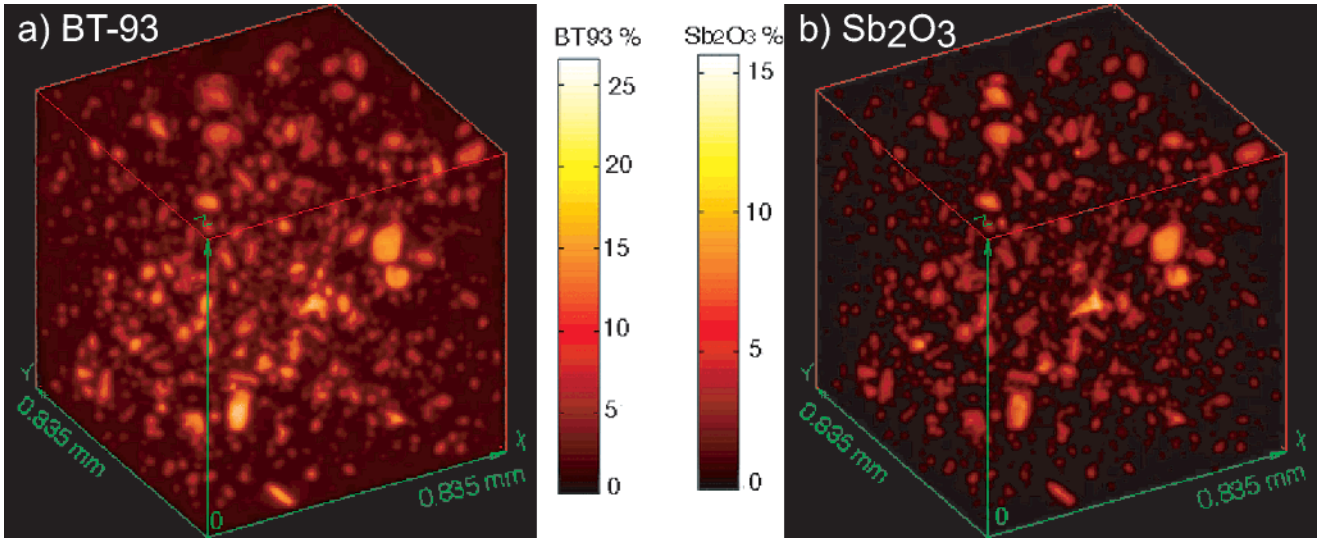

Figure 8. Rendered views of (a) BT-93 and (b) Sb_2O_3 concentrations as obtained from a constrained least-squares fit to tomography images acquired at seven different X-ray energies. The color bars are in units of vol %.

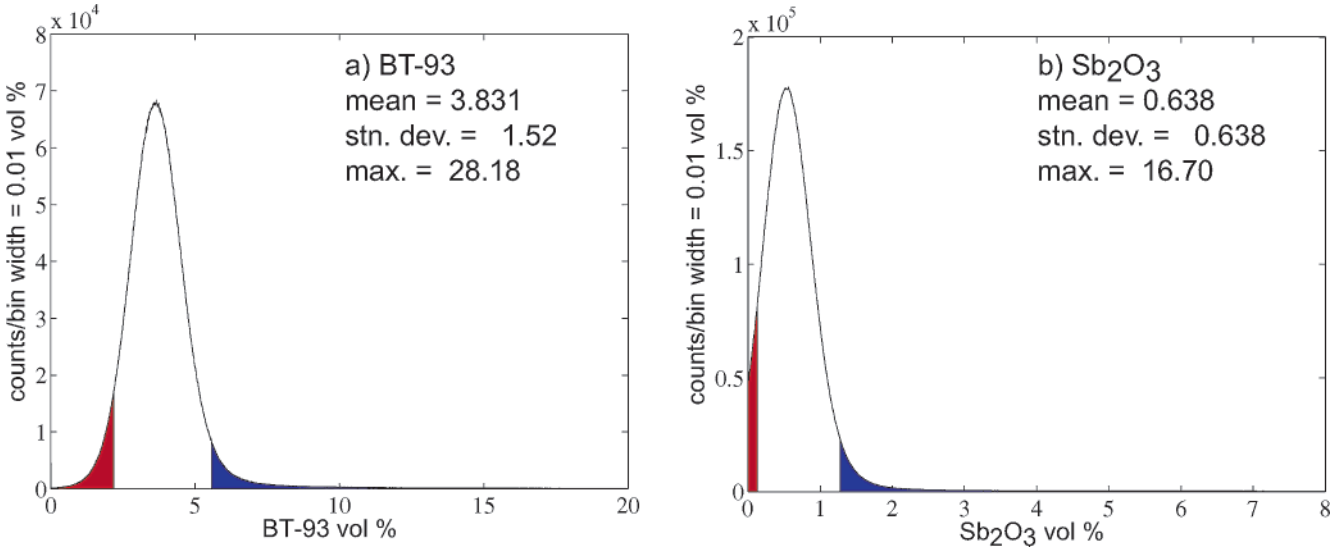

Figure 9. Histograms of (a) BT-93 and (b) Sb_2O_3 concentrations in vol %. The red highlighted region encompasses 5% of all voxels; similarly, the blue region shows another 5% of all voxels. These voxels will be visualized and counted in subsequent figures.

extremely high correlation between the flame retardant and its synergist with the most probable correlation at 3.2 vol % BT-93 and 0.4 vol % Sb_2O_3. The distance scale for the correlation is 3.34 μm and is set by the resolution of the tomography experiment. The high positive correlation reflects with the blending process; the flame retardant and its synergist are premixed and then blended with high impact polystyrene.

Concentration Distribution. The concentration distribution is visualized by creating isosurfaces at specific concentrations, thus showing domains with very small flame retardant concentrations and domains with very large concentrations. The histograms, Figure 9, are used to set the threshold concentrations, with the concentration distribution split into three ranges: (a) the 5% of voxels with the lowest concentrations of BT-93 or Sb_2O_3, (b) the 5% of voxels with the greatest concentrations of BT-93 or Sb_2O_3, and (c) the remaining 90% of voxels. Table 4 lists the concentration ranges and the fraction of voxels in each range; the deviation from

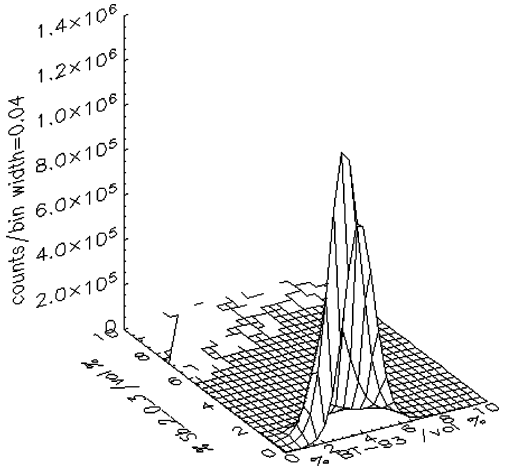

Figure 10. Contour plot showing a positive correlation between BT-93 and Sb_2O_3 concentrations; bin width = (0.04 vol %)^2. The maximum correlation occurs at 3.2 vol % BT-93 and 0.4 vol % Sb_2O_3.

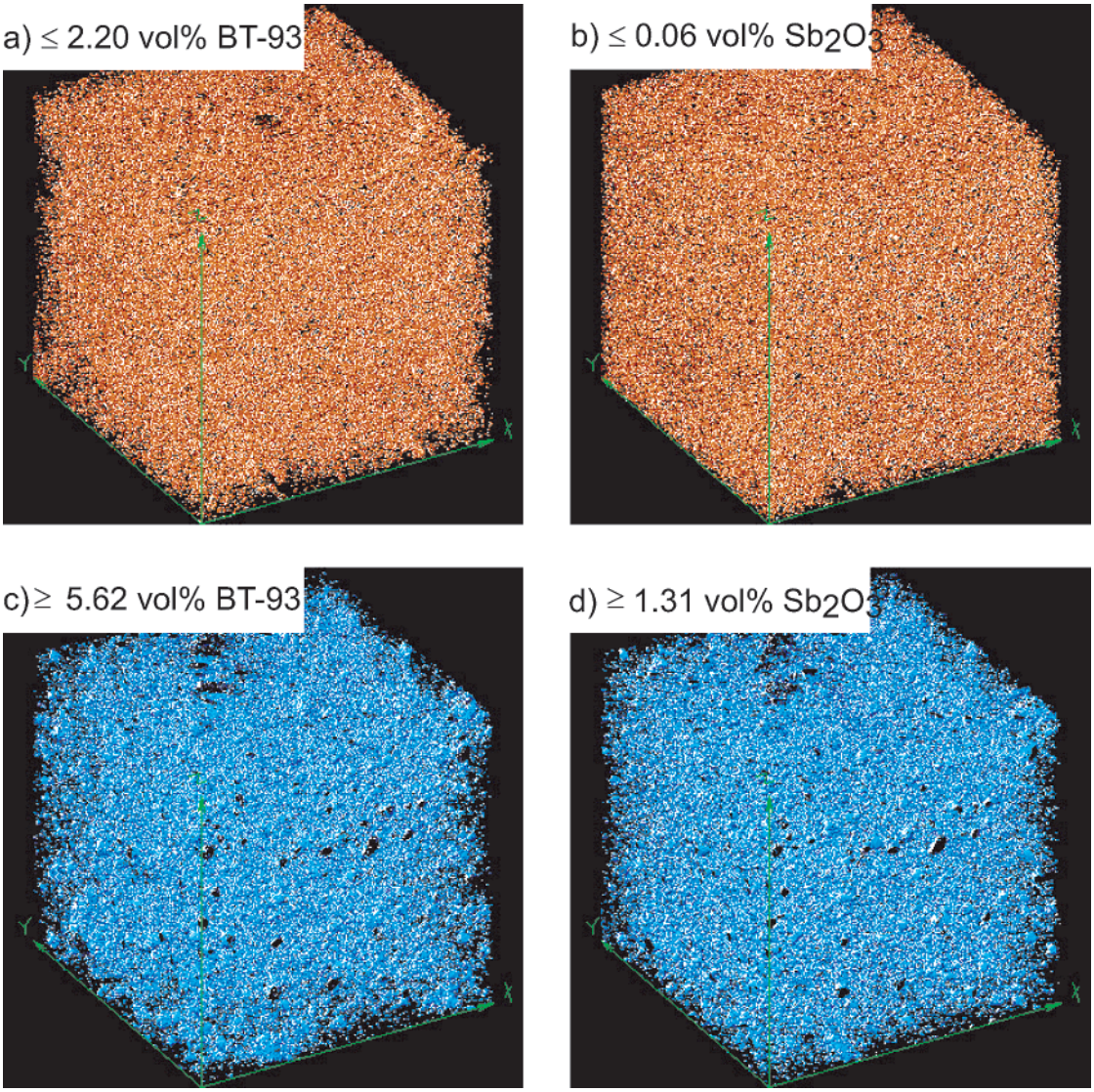

Figure 11. Volume renderings of domains with low and high concentrations of flame retardant. In each image, the threshold value is arbitrarily set to show 5% of all voxels. Domains of low flame retardant concentration are shown in red: (a) ≤2.2 vol % BT-93 and (b) ≤0.06 vol % Sb_2O_3. Domains of high flame retardant concentration are shown in blue: (a) ≥5.62 vol % BT-93 and (b) ≥1.31 vol % Sb_2O_3.

Table 4. Concentration Distribution of BT-93 and Sb_2O_3

			avg concentration/vol %	
	concentration/ vol %	% of voxels	tomography	chemical analysis
BT-93	≤2.20	5.4	3.831	4.25
	2.21−5.61	89.9		
	≥5.62	4.7		
Sb_2O_3	≤0.06	7.4	0.638	0.714
	0.07−1.30	88.0		
	≥1.31	4.6		

exactly 5% or 90% is a consequence of a particle size analysis program, 3DMA, which operates on 8-bit integer data rather a numerical representation with a larger dynamic range.

The splitting of the concentration distribution into lowest 5%, middle 90%, and greatest 5% is arbitrary. We admit that a more logical segmentation would be based on both the minimum flame retardant concentration needed to suppress a flame and the maximum flame retardant concentration beyond which no further improvement in performance is gained. However, data of this detail are not yet available, thus, the 5:90:5 vol % split.

As a memory aid, the next two figures are color coded. "Red" denotes voxels with the lowest concentrations; red is chosen because of its connection with safety. Conversely, voxels with the highest concentrations are shown in "blue", a cold color, suggestive of "cold, hard cash". Excessively high concentrations indicate waste of an expensive product, the flame retardant. Table 4 lists the concentration ranges and the fraction of voxels within each range; the fractions are close to the 5:90:5 vol % target.

Figure 11 shows renderings of the voxels having low and high concentration of BT-93 and Sb_2O_3. These renderings show that domains of low concentrations, Figures 11a and 11b, are randomly dispersed and probably very small. Similarly, the domains of high concentration, Figures 11c and 11d, are also randomly dispersed, though appear to be somewhat larger, indicating incomplete blending of the flame retardant into the polystyrene matrix. We note that roughly 90% of

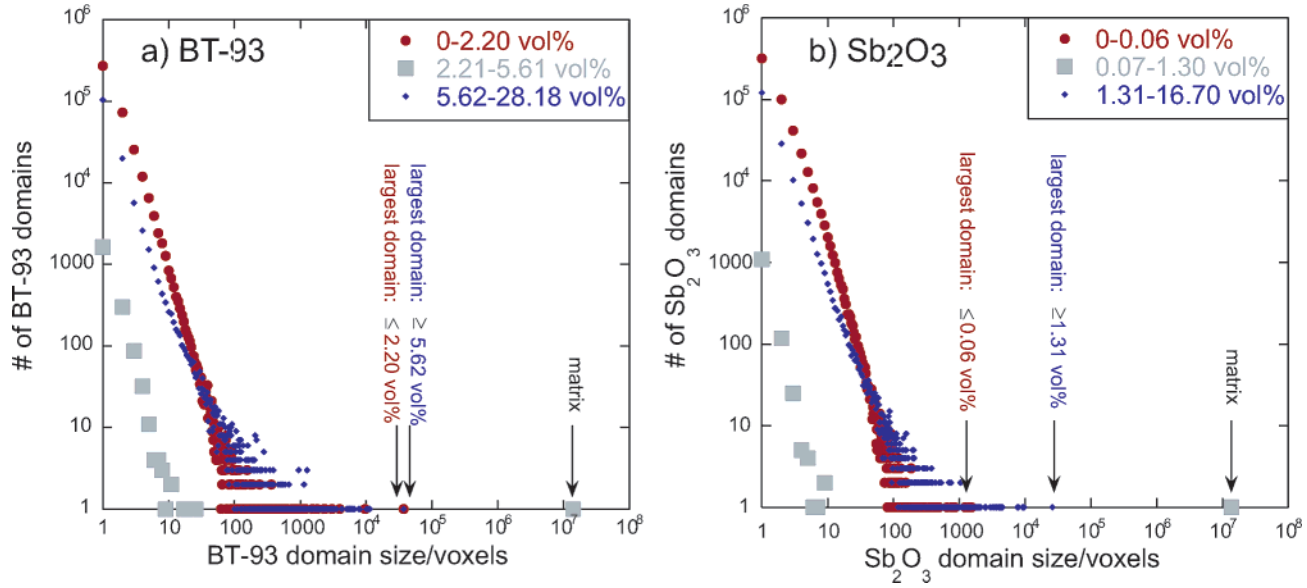

Figure 12. Domain size distribution of (a) BT-93 and (b) Sb_2O_3 within the subvolume, divided into three ranges: voxels with low (red), average, and high (blue) concentrations of the flame retardant. Nearly 90% of all voxels are in a single, interlinked domain labeled "matrix".

the voxels are not shown in these images; even when only 5% of the voxels are shown, a random distribution of voxels can create a dense object such as the cubes shown here. To gain further insight into the blending of the flame retardants, the domains are treated as particles and a particle size distribution is performed.

Figure 12 shows the results of six successive particle size distribution analyses applied to the BT-93 and Sb_2O_3 concentration distributions. For each analysis, the volume data set was converted to a binary data set, with "1" for each voxel with a concentration in the range of interest and "0" for voxels outside the range of interest. Again, the concentration ranges originate from the histograms, Figure 9, and are listed in Table 4. Of the 15 625 000 voxels in the subvolume, the largest single domain is the well-blended phase labeled "matrix" in the figures; for BT-93, this domain is 89% of the subvolume and, for Sb_2O_3, the matrix domain is 88% of the subvolume, values as expected from the 5:90:5 vol % split used to define the concentration ranges. As noted in Figure 11a, the domains having low BT-93 concentrations appear small, and this is verified with the particle size distribution. The largest domain with low BT-93 concentration has a volume of 37 284 voxels, corresponding to 0.001 mm^3 or 0.2% of the subvolume; this domain is labeled in Figure 12. Even better, the largest domain having low Sb_2O_3 concentration has a volume of only 1527 voxels, 6×10^{-5} mm^3. The domains with high flame retardant concentrations are slightly larger. For BT-93, there is one domain with a volume of 37 461 voxels having higher concentration than the well-blended phase. Likewise, for Sb_2O_3, there is one high concentration domain, labeled in Figure 12, with a volume of 26 004 voxels.

The last issue is whether the subvolume represents a sufficiently large volume so as to provide an accurate measure of the bulk composition. The flame retardant concentrations measured with tomography are 9.9% (BT-93) and 10.6% (Sb_2O_3) below the traditional chemical measurements (Table 4). On one hand, the particle size distribution (Figure 12) indicates a sufficiently large subvolume. For example, the largest domain of a high-concentration phase is only 0.2% of the subvolume; had there been two such domains in the subvolume, the bulk concentration would have increased by only 0.01%. On the other hand, the raw data as shown in Figure 2 clearly show a domain of extremely high flame retardant concentration lying just outside the subvolume. Inclusion of this domain in the subvolume would have pushed the concentration much higher, even exceeding the chemical measurement bulk value. As high-resolution, three-dimensional chemical analysis progresses from 250^3 to 1024^3 and larger data sets, we expect rapid convergence of average tomographic composition with traditional chemical analysis.

Conclusions

Three-dimensional chemical analysis at near micrometer resolution is demonstrated with multiple data sets acquired by synchrotron tomography. Tomography is performed at seven different X-ray energies, spanning Br and Sb absorption edges. The experimental X-ray absorption is fitted to a linear absorption model based on calculated mass linear attenuation coefficients, yielding the concentration distributions of a brominated aromatic, 3,3′,4,4′,5,5′,6,6′-octabromo-*N*,*N*′-ethylene-diphthalimide (Saytex BT-93), and antimony oxide, Sb_2O_3, within a matrix of high-impact polystyrene. The chemical distributions for BT-93 and Sb_2O_3 are visualized in 3D; histograms show the concentration distribution of each substance; the correlation between BT-93 and Sb_2O_3 concentrations is correlated with the sample preparation; and the effectiveness and economy of these flame retardants is explored with views of domains having lower and higher concentrations. Remarkably, all of these results were acquired with only 8 h of tomography instrument time.

Three-dimensional chemical analysis is shown here as an effective method for studying a blending process. The extension to nanoparticles embedded in a matrix is one of many possible applications, requiring modest

improvements in tomographic spatial resolution while still maintaining a macroscopic field of view.

Acknowledgment. The authors acknowledge the financial support from the Petroleum Research Fund administered by the American Chemical Society and from the Louisiana Board of Regents. Use of the Advanced Photon Source was supported by the U.S. Department of Energy, Basic Energy Sciences, Office of Science, under Contract No W-31-109-Eng-38.

CM0350333